Research Square

Preprints are preliminary reports that have not undergone peer review.
They should not be considered conclusive, used to inform clinical practice,
or referenced by the media as validated information.

# Polymer-modified Manganese ferrite composites for non-photonic degradation of Acid orange 10 dye from aqueous solution

**Anto Hepzibha**
V.O.Chidambaram College
**Paramasivam Rajakani**
prkvoc@gmail.com

V.O.Chidambaram College
**Chinnapiyan Vedhi**
V.O.Chidambaram College

**Research Article**

**Keywords:** Manganese ferrite composites, synthetic polymer, biopolymer, azo dye degradation, non-photonic method

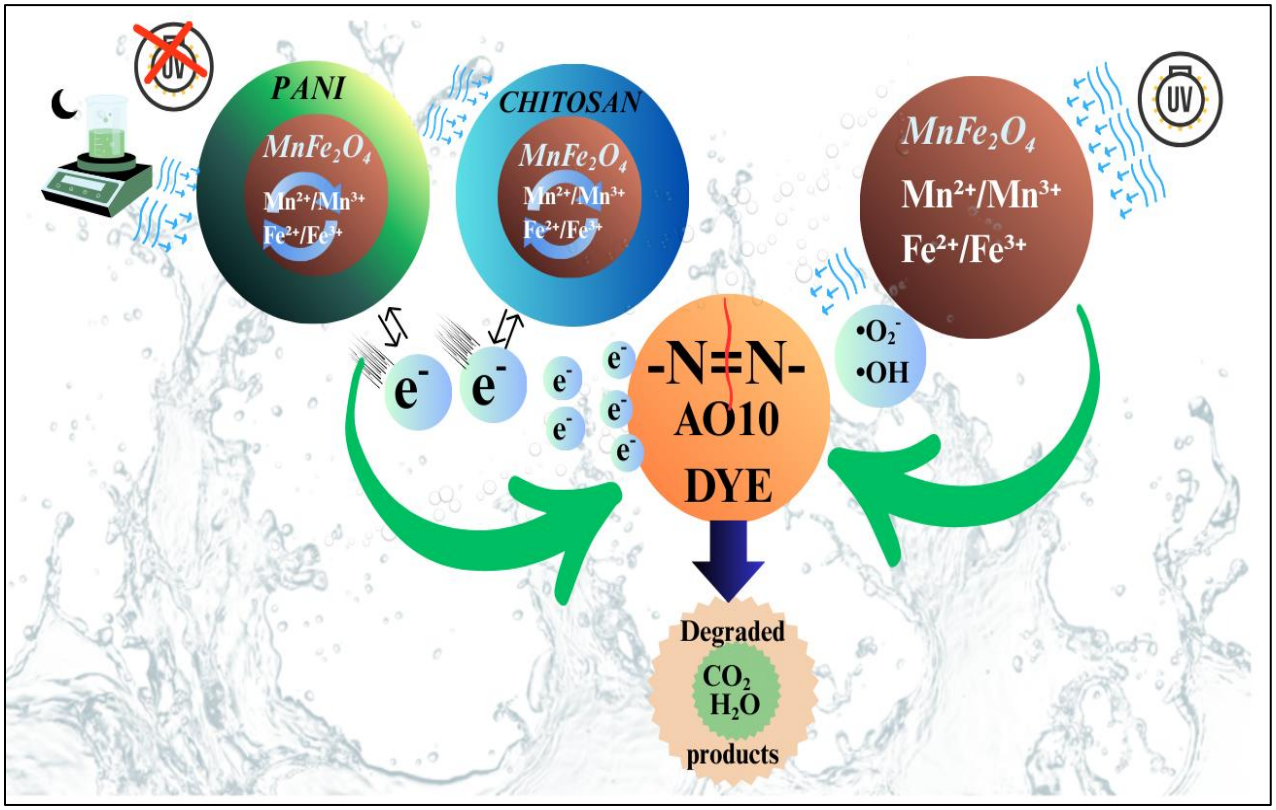
**Posted Date:** June 1st, 2026

**DOI:** https://doi.org/10.21203/rs.3.rs-9067352/v1

**License:** This work is licensed under a Creative Commons Attribution 4.0 International License.
Read Full License

# Polymer-modified Manganese ferrite composites for non-photonic degradation of Acid orange 10 dye from aqueous solution

**Anto Hepzibah[1][2], Paramasivam Rajakani[2]*, Chinnapiyan Vedhi[2]**




[1] A. Hepzibah, Research Scholar, Reg.No: 22212232032006, Affiliated by Manonmaniam Sundaranar University, Abishekapatti, Tirunelveli—627012, Tamil Nadu, India

[2] PG & Research Department of Chemistry,
V.O. Chidambaram College, Thoothukudi—628008, Tamil Nadu, India.
Affiliated to Manonmaniam Sundaranar University, Abishekapatti, Tirunelveli—627012, Tamil Nadu, India.

* E-mail: prkvoc@gmail.com

ORCID ID

[1] Anto Hepzibah https://orcid.org/0009-0005-9342-6549

[2]*Paramasivam Rajakani https://orcid.org/0000-0002-9832-9378

[2] Chinnapiyan Vedhi https://orcid.org/0000-0002-3446-0641

## Abstract

A superior performance of manganese ferrite modified with synthetic polymer, polyaniline and biopolymer, chitosan has been effectively developed to achieve, the degradation of an azo dye known as Acid orange 10, in dark conditions. Since the persistent azo dyes are not easily broken down by regular treatment methods as they are chemically Hard-to-degrade, where these azo dye industrial effluents remain a significant issue of environmental concern. In this investigation, Manganese ferrite (MF), $MnFe_2O_4$/polyaniline (MF/PANI), and $MnFe_2O_4$/chitosan (MF/CS) nanocomposites were used to determine the photonic and non-photonic degradation of Acid Orange 10 (AO10) dye under ambient dark stirring conditions. The structural, morphological and surface chemical properties of the catalysts were analyzed with Fourier transform-infrared spectroscopy (FTIR), X-ray diffraction (XRD), ultra violet visible spectroscopy (UV-Vis), the high-resolution transmission electron microscopy (HRTEM), energy dispersive X-ray analysis (EDX), X-ray photoelectron spectroscopy (XPS), Brunauer-Emmett-Teller (BET) surface area analysis and Barrett-Joyner-Halenda (BJH) pore size distribution. The UV-analysis for the dye degradation resulted with 65% in 20 mins under UV-photoreactor for base MF, and 98.5% in 6 mins for MF/PANI and 95.8% in 14 mins for MF/CS nanocomposites from aqueous solution under dark stirring conditions.

**Key words** Manganese ferrite composites, synthetic polymer, biopolymer, azo dye degradation, non-photonic method

## Introduction

Rapid industrialization and the heavy use of synthetic dyes in the textile, leather and food industry have led to high amounts of colored wastewater, which are extremely threatening the water resources (Akter and Dong 2024). Acid orange 10 (AO10) is an azo dye, especially persistent, with the addition of stable -N=N- chromophoric linkage and aromatic substituents, and is not susceptible to normal biological and photolytic processing (Nessaibia et al. 2023). As such, the major challenge in wastewater treatment is to come up with effective and environmentally friendly catalysts that can break up such uncooperative dyes under mild conditions. The heterogeneous catalytic degradation on the basis of transition-metal ferrites ($MFe_2O_4$; M=Mn, Zn, Co, Ni, etc.) has been a promising direction due to its own spinel structure, redox controllable characteristic and easy magnetic separation (Suresh et al. 2025). The presence of mixed-valence $Fe^{2+}/Fe^{3+}$ and $Mn^{2+}/Mn^{3+}$ ions, which promote effective electron transfer and reactive oxygen species (ROS) generation, makes Manganese ferrite (MF) particularly interesting among them (Manohar et al. 2025). Nevertheless, pure $MnFe_2O_4$ nanoparticles usually experience aggregation, low concentration of surface-active sites and slow electron transport and this limits their catalytic ability (Skliri et al. 2021). In order to overcome such shortcomings, encapsulation of polymer strategies have been considered in order to improve the dispersion, stability and catalytic activity of ferrites (Sambhudevan 2021). Polyaniline (PANI) is a synthetic conducting polymer, which

offers conjugated π-electron network, which separates charge and improves the movement of electrons, which in turn facilitates redox cycling during catalysis (Molapo et al. 2012). Additionally, by coordinating with metal centers, its nitrogen functionalities can enhance catalytic reactivity and interfacial contact. Contrarily, chitosan, a natural biopolymer of chitin, adds a large amount of the functional groups of -OH and -$NH_2$, which are involved not only in the stabilization of ferrite nanoparticles but also in the adsorption of dyes by hydrogen bonds and electrostatic forces (Chen et al. 2020). MF, MF/PANI, and MF/Chitosan composites have been prepared and experimentally studied extensively in the current work as catalysts of the non-photonic degradation of Acid Orange 10 dye under simple stirring conditions, without any external light irradiation or chemical oxidants. Where the traditional degradation methods, even though effective, they often depend on photonic energy sources (Peleyeju and Arotiba 2018), which limits their usage in regions of dark and turbid waste water. But this type of non-photonic process is a huge step forward in that it employs intrinsic redox, and surface catalytic capabilities of the composites at a low temperature to induce the degradation of dyes in ambient, dark conditions. The presence of synergy between $MnFe_2O_4$ and the polymeric framework is likely to help with better charge transfer, greater dye adsorption, and quicker degradation rates (Das et al. 2020). In-depth physicochemical characterizations- FTIR, XRD, UV- Vis, HRTEM, EDX, BET and XPS were used to clarify the structural, morphological and surface characteristics of the synthesized catalysts. This paper would tend to match the compositional and surface characteristics with the catalytic performance and to develop a mechanistic interpretation of the non-photonic degradation route of the Acid Orange 10 dye. The results shows that polymer-modified ferrite composites have the potential to be effective, sustainable, and reusable catalysts for wastewater treatment applications.

## 1. Materials and synthesis methods

### 1.1. Materials

$Fe(NO_3)_3 \cdot 9H_2O$, $Mn(NO_3)_2 \cdot 4H_2O$ and NaOH, Aniline (99.9% v/v), hydrochloric acid (HCl, 35% v/v), ammonium persulfate [$(NH_4)_2S_2O_8$], chitosan, 25 wt % aqueous glutaraldehyde were supplied by Merck Chemicals Ltd.

### 1.2. *Synthesis of $MnFe_2O_4$ Nanoparticles*

A traditional co-precipitation technique was used to synthesize Manganese ferrite (MF) nanoparticles (Fig.1). Solution A was first made by dissolving 0.89 g of manganese nitrate tetrahydrate [$Mn(NO_3)_2 \cdot 4H_2O$] in 50 mL of deionized water. Solution B was obtained by dissolving 2.82 g of ferric nitrate nonahydrate [$Fe(NO_3)_3 \cdot 9H_2O$] in 50 mL of deionized water separately. To ensure homogenization, solution A was then gradually added to solution B while being constantly stirred. After heating the mixture to 70 °C, a 2 M sodium hydroxide (NaOH) solution was gradually

added until the reaction mixture's pH is 13. For one hour, the resultant suspension was continuously stirred at 70 °C to enable full precipitation and the formation of $MnFeO_4$ nanoparticles. And the obtained ferrite nanoparticles are washed with ethanol and deionized water and further calcined at 600ºC for 5 hours (Zolfaghari et al. 2021).

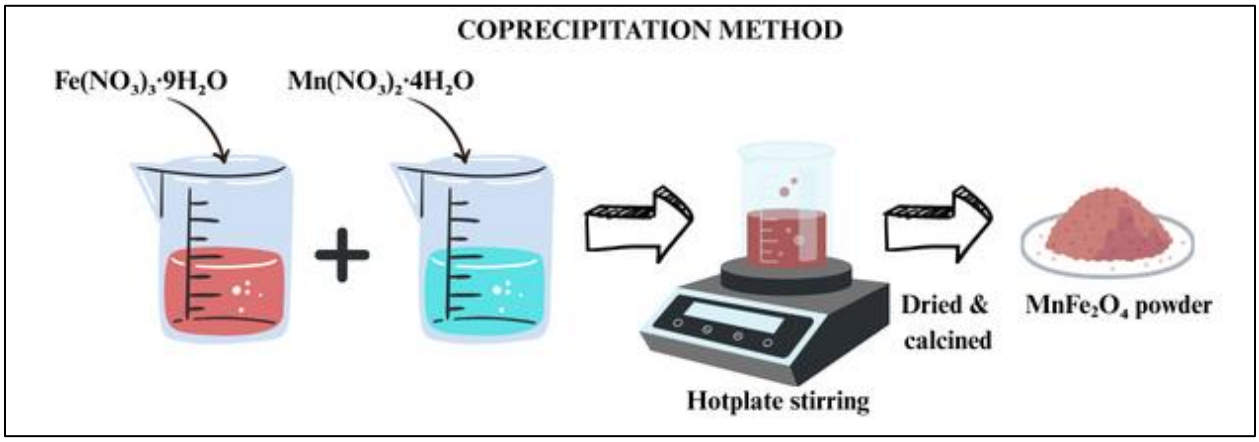



**Figure 1.** Coprecipitation method for synthesis of $MnFe_2O_4$

### 1.3.*Synthesis of $MnFe_2O_4$/Polyaniline (MF/PANI) Composite Synthesis*

In situ oxidative polymerization of aniline in the presence of $MnFe_2O_4$ (MF) nanoparticles produced the $MnFe_2O_4$/Polyaniline (MF/PANI) composite (Fig.2). Typically, bath sonication was used to disperse 120 mg of $MnFe_2O_4$ nanoparticles in 10 mL of 1 M HCl solution in order to get uniform suspension. And separately, 80 mL of ice-cooled 1 M HCl solution was continuously stirred while 0.19 mL of freshly distilled aniline monomer was dissolved. The aniline solution was then gradually stirred while 10 mL of 1 M HCl containing 570 mg of ammonium persulfate [$(NH_4)_2S_2O_8$], an oxidizing agent, was added dropwise. After adding the MF nanoparticle dispersion to the reaction mixture, the polymerization was left to continue for 12 hours at a temperature between 0ºC and 5 °C while being constantly stirred. To obtain the final MF/PANI composite, the resulting dark-green precipitate was collected by filtration, thoroughly cleaned with ethanol and deionized water until the filtrate became colorless, and then dried at 60 °C for 12 hours (Khilari et al. 2015).

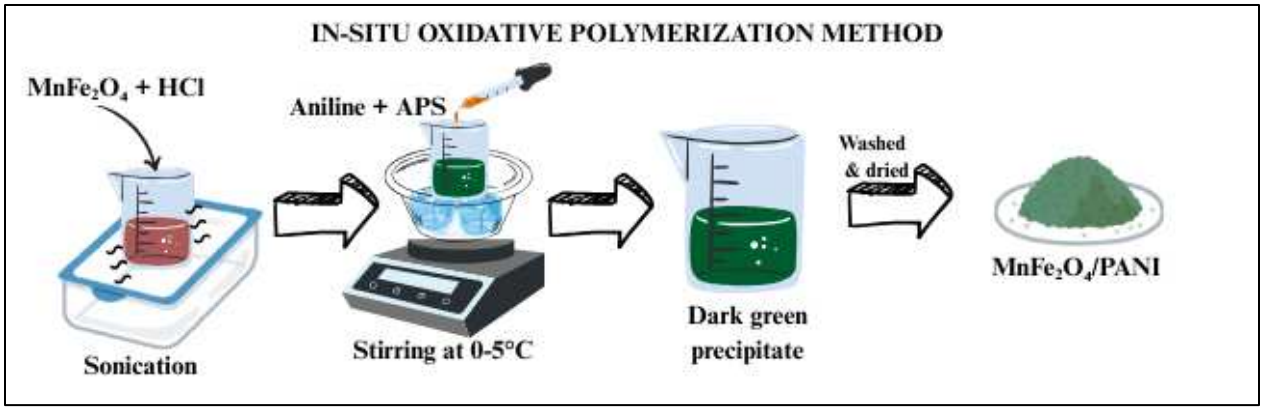



**Figure 2.** Synthesis method for $MnFe_2O_4$/PANI composite

### 1.4.*Synthesis of $MnFe_2O_4$/Chitosan (MF/CS) Composite*

$MnFe_2O_4$ nanoparticles were crosslinked within a chitosan matrix to create the $MnFe_2O_4$/Chitosan (MF/CS) composite (Fig.3). A standard synthesis involved dispersing 0.2 g of $MnFe_2O_4$ nanoparticles in 20 mL of a pre-made chitosan solution while stirring constantly to guarantee even dispersion of the nanoparticles. Then, as a crosslinking agent, 0.5 mL of a 25 wt % aqueous glutaraldehyde solution was added dropwise to the mixture. For six hours, the reaction mixture was agitated at room temperature to promote the development of a network between the ferrite nanoparticles and the chitosan chains. To get the MF/Chitosan composite, the resultant product was separated by centrifugation, repeatedly cleaned with ethanol and acetone to get rid of unreacted species and leftover glutaraldehyde, and then dried at 60 °C (Xiao et al. 2013).

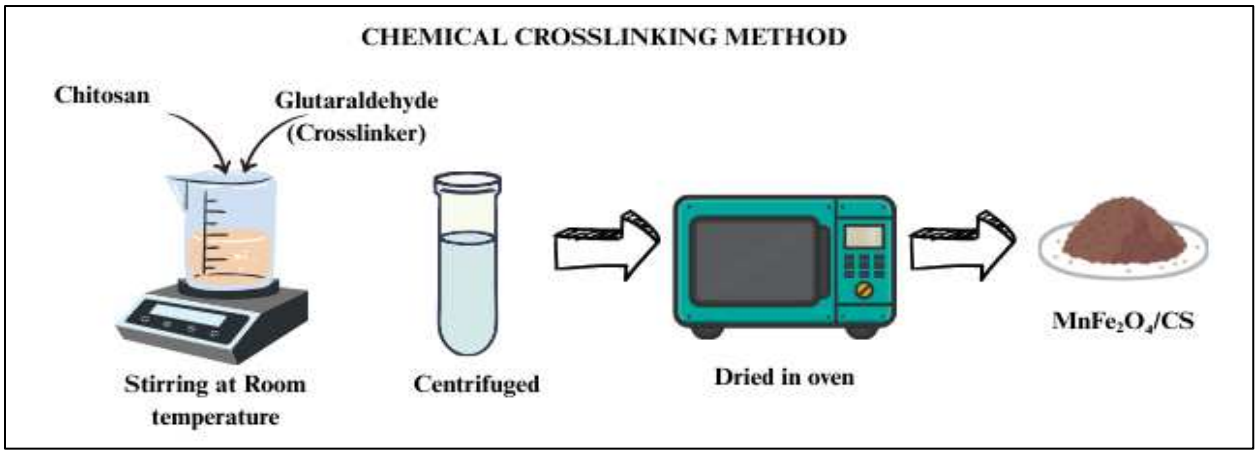



**Figure 3.** Synthesis of $MnFe_2O_4$/Chitosan composite

## 2. Results and discussion

### 2.1. Fourier Transform Infrared spectroscopy (FTIR)

The FTIR Spectra for MF, MF/PANI, MF/CS are shown in the Fig. 4a for pure metal ferrite the peaks at 380–400 and 441 $cm^{-1}$ corresponds to Fe–O stretching at octahedral sites of the spinel structure, commonly assigned to manganese ferrite in this region (Ilosvai et al. 2025). And the peak at 550-610 $cm^{-1}$ is associated with Fe–O stretching at tetrahedral sites, and Mn-O bonds which is the characteristic for the spinel-type ferrite frameworks. And the observed peak at 833 $cm^{-1}$ is attributed to out-of-plane and in-plane aromatic C-H bonds (Giannousi et al. 2025), 1366 $cm^{-1}$, 1797 $cm^{-1}$ and 3480-3600 $cm^{-1}$ peaks are attributed to O–H in-plane bending and C=O stretching vibrations and surface water adsorption (Duarte et al. 2022) and finally the peaks at 2425, 2756, 2839 $cm^{-1}$ corresponds to the C–H stretching vibrations in the pure manganese ferrite (Ilosvai et al. 2025). In Fig.4b polyaniline modified metal ferrite (MF/PANI), the peaks at 1116, 1140 $cm^{-1}$ corresponds to the "electronic-like band" and is the vibration of N=Q=N(Q) represents a quinone ring in polyaniline (Meng et al. 2016). And 1295 $cm^{-1}$ is attributed to for benzenoid, 1247 $cm^{-1}$ for quinoid units which verifies the polyaniline's bi-polaron state and aromatic ring substitutions(Meng et al. 2016). And the peaks at 1486, 1570 $cm^{-1}$ corresponds to C=C stretching of the benzenoid and quinoid segments in polyaniline, which are the principal signature peaks for oxidized and conducting forms (Kolhar et al. 2023). From the Fig.4c the peaks at 1025, 1072 $cm^{-1}$ are attributed to C–O skeletal stretching vibrations in the chitosan backbone, and the NH bending, particularly from glycosidic bonds linking glucosamine units and 1036, 2870 $cm^{-1}$ corresponds to the ring bending, $CH_2$ aliphatic stretching,(Itodo et al. 2017; Vigneshwari and Gokula). And the 1388 $cm^{-1}$, 1531, 1570 $cm^{-1}$, are related to $CH_2$ bending present in chitosan N–H bending or amide II bands (from chitosan's deacetylated fragments), as well as deformation vibrations of the $NH_2$ groups, and 1650 $cm^{-1}$ is assigned to amide I (C=O stretching vibration of the chitosan backbone) (Doğan 2020). Thus, the FTIR spectrum confirms the modification with the metal ferrite with its synthetic and biopolymers relating to its functional groups. And these observations correspond to the structural integrity and successful functionalization of the surface of the composites. Fig. 4 a, b, c depicts the FTIR Spectrums of base manganese ferrite (MF) and its synthetic and biopolymer composites such as MF/PANI, MF/CS.

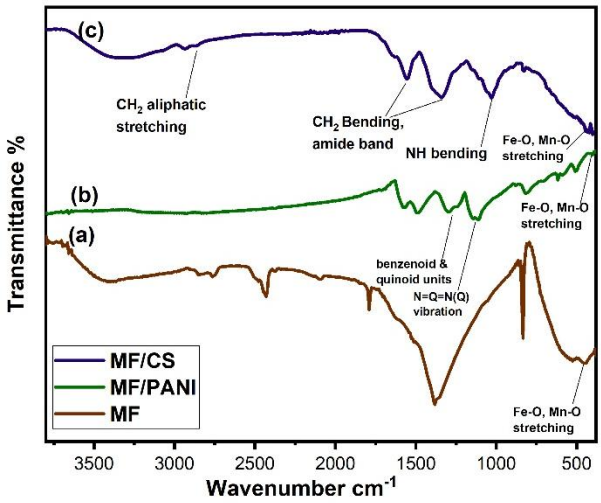



**Figure 4.** FTIR Spectrum of (a) Manganese ferrite, (b) Manganese ferrite/polyaniline, (c) Manganese ferrite/chitosan composites

### 2.2.Powder X-ray diffraction analysis

**Fig 5.** a. shows the XRD patterns of pure Manganese ferrite (MF), Manganese ferrite/polyaniline (MF/PANI), and Manganese ferrite/chitosan (MF/CS) nanocomposites. The cubic spinel structure of $MnFe_2O_4$ matches well with the (JCPDS #74-2403) and the major peaks at 2θ = 29.6°, 35.7°, 39.2°, 42.7°, 48.1°, 54.3°, and 62.6°, corresponding to the (220), (311), (400), (422), (333), (531), and (620) planes, respectively (Devi and Soibam 2017). And in **Fig 5 b.** the values at 2θ = 18.6°, 25.6°corresponds to (111), (101) plane (Zeng et al. 2016) which are the characteristic peaks of PANI (Abdollahi et al. 2020), and 32.9° represents the major $MnFe_2O_4$ spinel peak (Meng et al. 2016; Patil et al. 2023). And in the **Fig 5 c.** the diffraction peaks at 2θ = 29.78, 35.9, 56.4, represents the (220), (311), (511) planes (Lahouti and Naeimi 2020) and the values at 33.47°, 49.8°, 54.2° indicates the formation of cubic spinel structure of $MnFe_2O_4$ (Mohammad Hosseini et al. 2025). The positive peak shift of $MnFe_2O_4$ from 29.6° to 32.9° (Fig.5b) which shows the lattice distortion induced by strong interfacial interactions between $MnFe_2O_4$ and polyaniline nanocomposite, this indicates the successful composite formation rather than simple physical mixing. In contrast, the MF/CS nanocomposite (Fig.5c) retained the 2θ values indicating the weaker lattice distortion because of the amorphous nature of chitosan. Therefore, on polymer incorporations, the peaks exhibit increased broadening and reduced intensity. Also, the maintained spinel structure shows the effective integration with its polymers.

The average Crystallite sizes (D) were estimated using the Debye Scherrer equation:

$$D=0.9\lambda/\beta\cos\theta \qquad \textbf{(Eqn. 1)}$$

where λ=1.5406Å (Cu $K\alpha_1$), β is the FWHM (in radians), and θ is the Bragg angle (in degrees). And the average crystallite sizes for MF is calculated to be 36.55 nm, MF/PANI is 59.88 nm, and MF/CS is 20.9 nm.

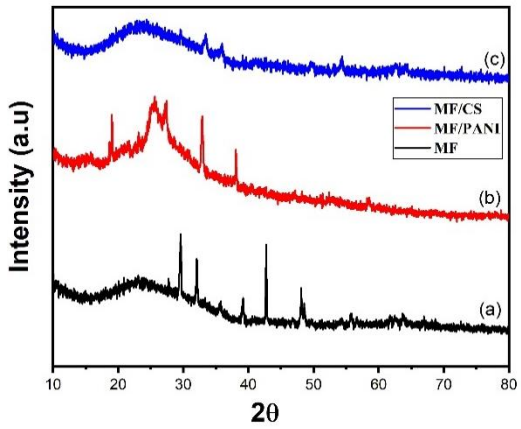



**Figure 5.** XRD Spectrum of (a) Manganese ferrite, (b) Manganese ferrite/polyaniline, (c) Manganese ferrite/chitosan composites

### 2.3.X-ray photoelectron spectroscopy analysis

The XPS spectroscopic analysis of $MnFe_2O_4$, $MnFe_2O_4$/PANI, $MnFe_2O_4$/Chitosan nanocomposites are shown in the Fig 6. the elemental composition and the oxidation states are calculate using the varying binding energies for different elements. Fig 6. represents the survey scan of the samples which determines the presence of the elements like carbon, nitrogen, oxygen, manganese and iron. All the spectra were calibrated using 284.8eV for C1s peak as the reference and the deconvoluted peaks were achieved using gaussian function with Shirley background baseline correction to conclude with the oxidation states of the elements.

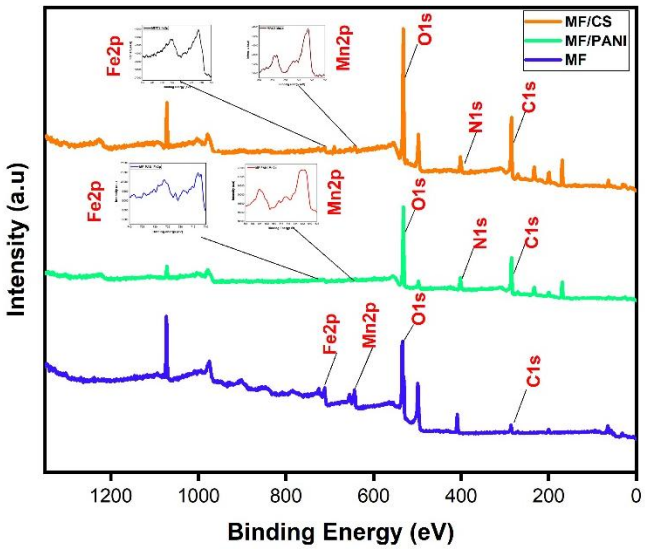



**Figure 6.** XPS survey spectra of MF, MF/PANI, MF/CS nanocomposites

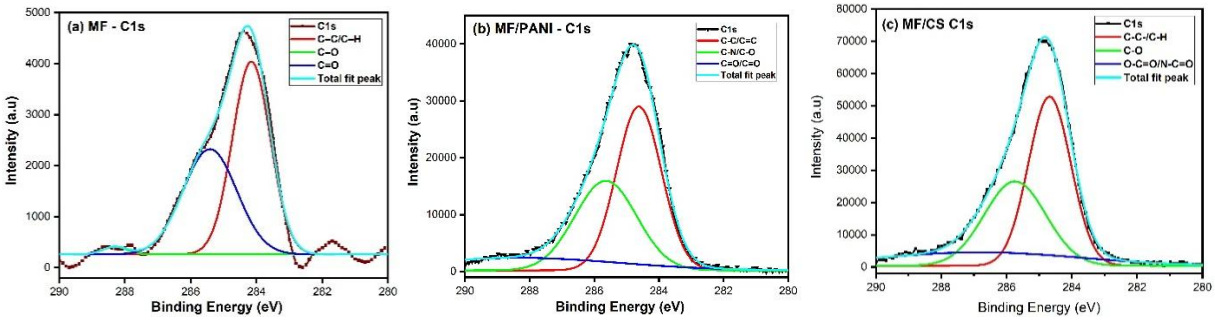



**Figure 7.** C1s XPS Spectra of (a) MF, (b) MF/PANI, (c) MF/CS nanocomposites

## C1s analysis

The C1s XPS spectra of pure $MnFe_2O_4$ in Fig.7a shows a dominant peak at 284.8eV, 286.2eV, 288.6eV which corresponds to the C-C/C-H bonds, C-O bonds, C=O carbonyl groups. For MF/PANI nanocomposite (Fig. 7b) the additional peaks at 284.6eV, 285.6eV, 288.1eV corresponds to the C-C/C=C, C-N/C-O, C=O/C=N bonds of the polyaniline backbone. Similarly, for MF/CS nanocomposite (Fig. 7c) the peaks at 285.7eV and 284.7eV represents the C-O and C-C/C-H of the chitosan components. Which reflects the strong interfacial interaction between the polymer backbone and the $MnFe_2O_4$ structure.

## Mn2p analysis

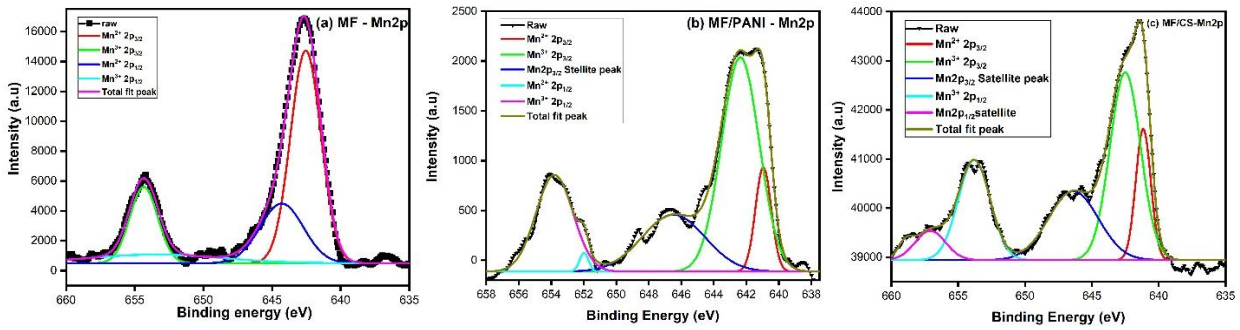



**Figure 8.** Mn2p XPS Spectra of (a) MF, (b) MF/PANI, (c) MF/CS nanocomposites

The Mn2p XPS spectra of $MnFe_2O_4$ in Fig.8a shows deconvoluted peaks at 642.5eV and 644.2eV $Mn^{2+}2p_{3/2}$ and $Mn^{3+}2p_{3/2}$, while the peaks at 652.8eV, 654.3eV represents the $Mn^{2+}2p_{1/2}$ and $Mn^{3+}2p_{1/2}$ which indicates the spinel structure. In Fig.8b for MF/PANI the peaks at 640.9eV, 642.3eV corresponds to the $Mn^{2+}2p_{3/2}$, $Mn^{3+}2p_{3/2}$ components also with the presence of the satellite peak at 646.4eV and also the peaks at 652eV, 653.8eV represents the $Mn2p_{1/2}$ components with $Mn^{2+}$ and $Mn^{3+}$ oxidation states, which shows the electronic interaction between the ferrite and PANI. Similarly, for MF/CS in Fig.8c the peaks at 641.1 eV, 642.4 eV indicates the $Mn^{2+}$ & $Mn^{3+}$ $2p_{3/2}$ and a satellite peak at 646.3eV, also the peaks at 653.8 eV, 657.1eV are assigned to $Mn2p_{1/2}$ components suggesting the strong incorporation of Mn ions with the chitosan functional groups.

On the whole the Mn2p spectra reveals the confirmation of $Mn^{2+}/Mn^{3+}$ oxidation states in all the composites (Biesinger et al. 2011).

**Fe2p analysis**

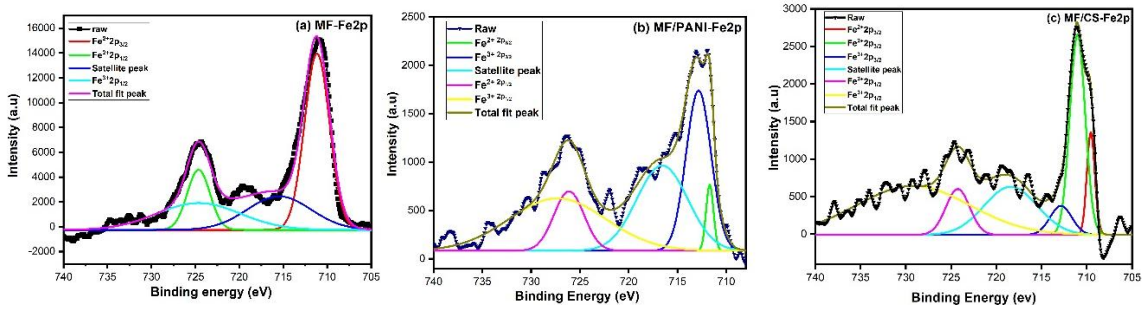



**Figure 9.** Fe2p XPS Spectra of (a) MF, (b) MF/PANI, (c) MF/CS nanocomposites

The Fe2p XPS spectra of $MnFe_2O_4$ in Fig.9a depicts the deconvoluted peaks at 711.08 eV which corresponds to $Fe^{2+}2p_{3/2}$ and 715.6eV represents the satellite peak and the peaks at higher binding energy 724.5eV, 725.6eV are attributed to the $2p_{1/2}$ components with $Fe^{2+}$ & $Fe^{3+}$ states, which are relevant with the spinel ferrite structure. In Fig.9b for MF/PANI the peaks at 711.6eV, 712.8eV are attributed to the $Fe2p_{3/2}$ component with $Fe^{2+}$ and $Fe^{3+}$ states along with the satellite peak at 716.5eV and the peaks at 726.2eV and 727.4eV $Fe2p_{1/2}$ states which shows the electronic interaction with the Fe ions and the PANI matrix. And for MF/CS (Fig.9c) the $Fe2p_{3/2}$ peaks at 709.8 eV, 711.08 eV, 712.9eV with $Fe^{2+}$ & $Fe^{3+}$ and the peaks at 724.24eV, 727.9eV are attributed to the $Fe2p_{1/2}$ components which show the interaction of chitosan functional groups with Fe ions. Thus, the Fe2p spectra confirms the presence of the mixed $Fe^{2+}/Fe^{3+}$ oxidation states and stronger interactions in all the composites (Grosvenor et al. 2004).

**O1s analysis**

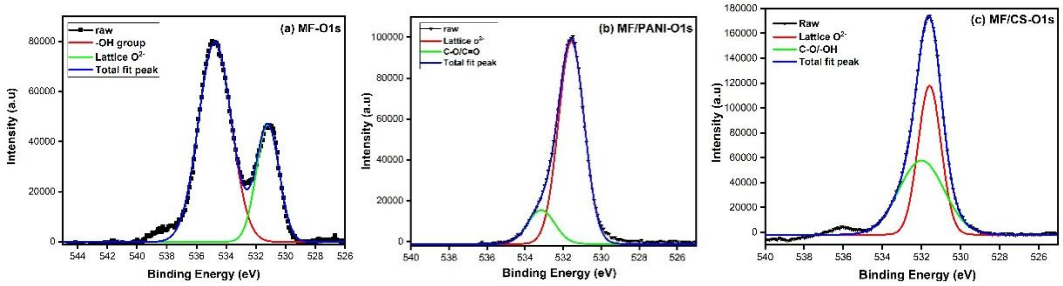



**Figure 10.** O1s XPS Spectra of a) MF, b) MF/PANI, c) MF/CS nanocomposites

The O1s XPS spectra of $MnFe_2O_4$ (Fig.10a) shows that the peaks at 531.17eV which corresponds to the lattice oxygen, $O^{2-}$ which is related to metal oxygen bonds in (Mn-O/Fe-O) in the spinel metal ferrite structure and 534.84eV corresponds to the hydroxyl groups (-OH). And in the Fig.10b for MF/PANI composite the peaks at 531.16eV represents the lattice oxygen and 533.18eV corresponds to the C-O/C=O of the PANI matrix. Similarly, for MF/CS composite (Fig.10c)

531.6eV shows the lattice oxygen and the peak at 532.1eV corresponds to the hydroxyl groups and C-O bonds in the chitosan polymer. The change in binding energy was observed in the polymer-modified composites which appear from oxygen containing functional groups of polyaniline and chitosan that are due to the polymer-ferrite interaction (Murugesan et al. 2021).\

**N1s analysis**

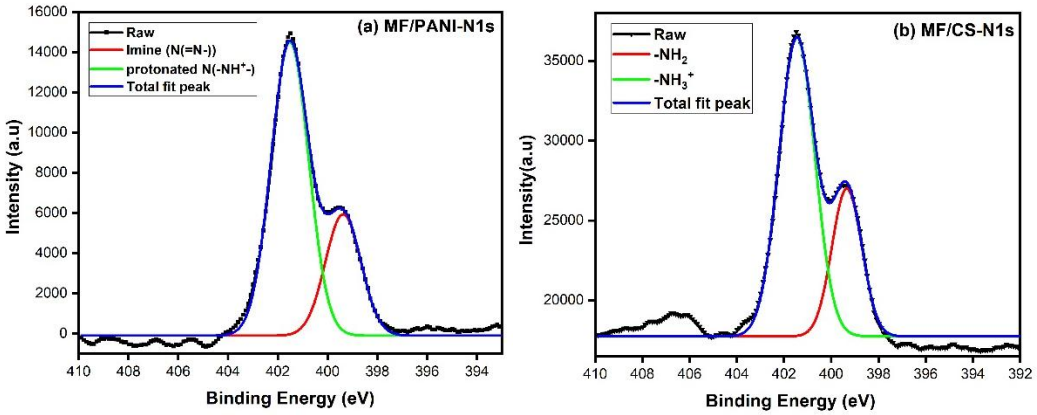



**Figure 11.** N1s XPS Spectra of a) $MnFe_2O_4$/PANI and b) $MnFe_2O_4$/CS nanocomposites

The N1s spectra for MF/PANI composite (Fig.11a), the observed peaks at 399.3eV corresponds to the amine/imine nitrogen (-NH-/=N-) which are related to the benzenoid and quinoid units of the polyaniline backbone and the peak at 401.5eV represents the protonated or positively charged nitrogen ($-NH^+-$) which shows the partial oxidation and doping of polyaniline into the ferrite. And for MF/CS composite (Fig.11b) the N1s peaks at 399.3eV and 401.4eV represents the amine nitrogen ($-NH_2$) and protonated amine species ($-NH_3^+$) from the biopolymer chitosan.

Overall, the XPS spectra of all the samples confirm the presence of Mn, Fe, O and C while N1s peak appear only in the polymer-modified composites, which validates the successful polymer incorporation into the ferrite nanoparticles (Vieira et al. 2011).

**2.4.High resolution transmission electron microscopic analysis and SAED pattern analysis**

The HRTEM images revealed the formation of nanoparticles which exhibited its morphology and the average particle size is also calculated. The HRTEM image of $MnFe_2O_4$ reveal a well-defined nanorod like structure with elongated structure and the gaussian histogram (Fig.15a) represents the average particle size of $MnFe_2O_4$ which is 7.23nm. And in the Fig. 12 it is well depicted that the nanorod morphology is preserved and the encapsulation of polymers into the nanorods can be seen. Also, the gaussian histograms finalizes the average particle size to be 33.42nm for (Fig.15b) MF/PANI and 24.85nm for MF/CS (Fig.15c). Overall, the HRTEM analysis confirms that both the polymers including polyaniline (Fig.13) and chitosan (Fig.14) are successfully incorporated into the $MnFe_2O_4$ nanorods. The Selected area electron diffraction of $MnFe_2O_4$ (Fig.16a) shows the

well-defined concentric diffraction rings that matches well with the interplanar spacings (111), (220), (400), (333), (444) of the JCPDS card number 01-74-2403, which confirms its polycrystalline nature and the formation of pure $MnFe_2O_4$. Similarly, for polymer coated $MnFe_2O_4$ the SAED patterns retains the diffraction rings of the manganese ferrite which indicates the incorporation of the polyaniline (Fig.16b) and the chitosan (Fig.16c) into the $MnFe_2O_4$ does not change the crystalline structure of the spinel ferrite. Also, the d-spacing values of the MF/PANI, MF/CS composites match well with the planes of the $MnFe_2O_4$.

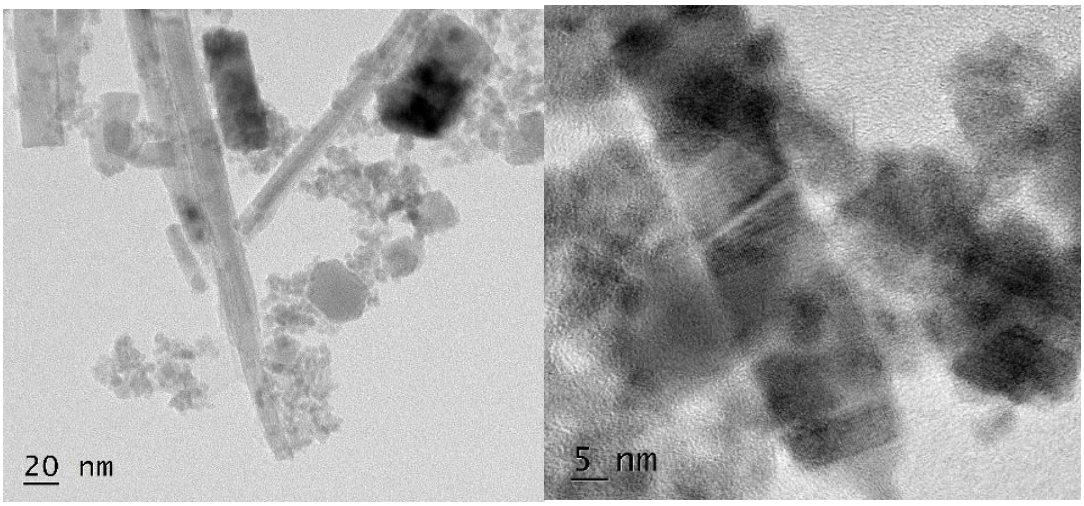



**Figure 12.** HRTEM images of $MnFe_2O_4$

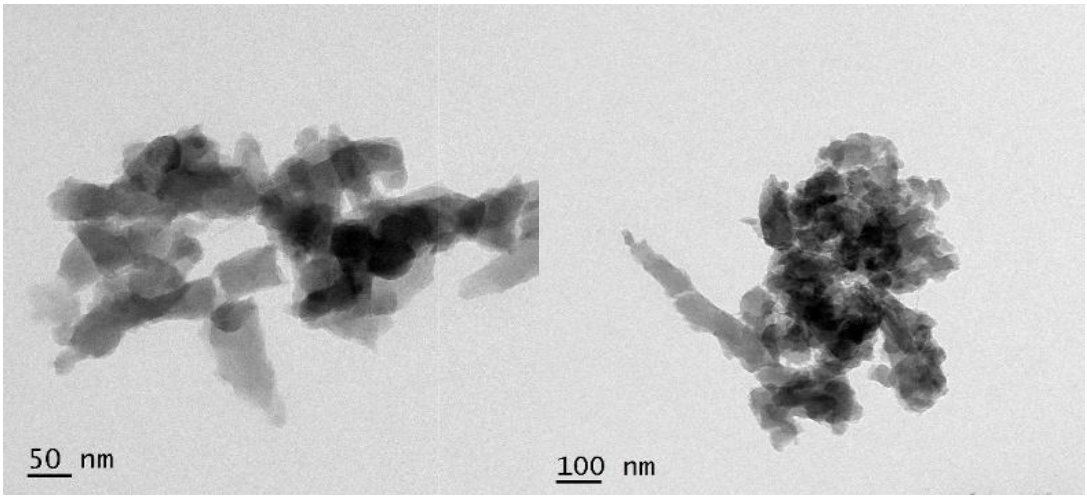



**Figure 13.** HRTEM images of $MnFe_2O_4$/PANI

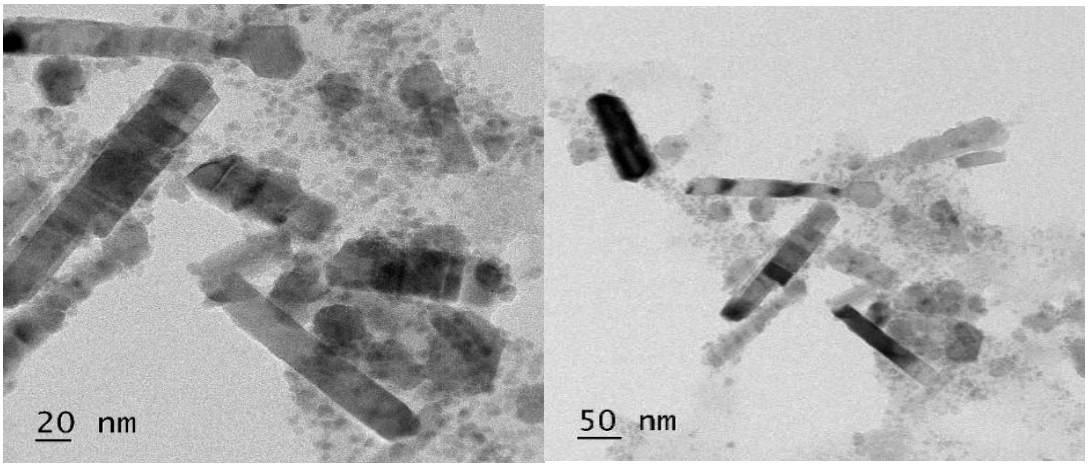



**Figure 14.** HRTEM images of $MnFe_2O_4$/CS

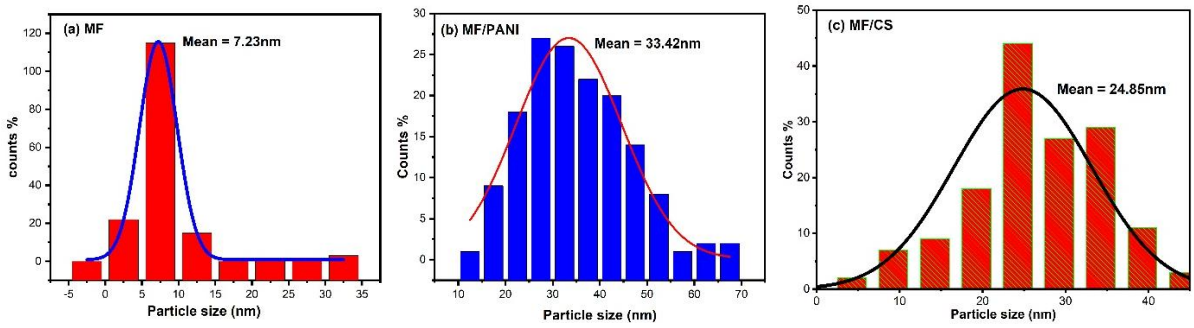



**Figure 15.** Gaussian histograms for particle size determination of (a) MF, (b) MF/PANI, (c) MF/CS nanocomposites

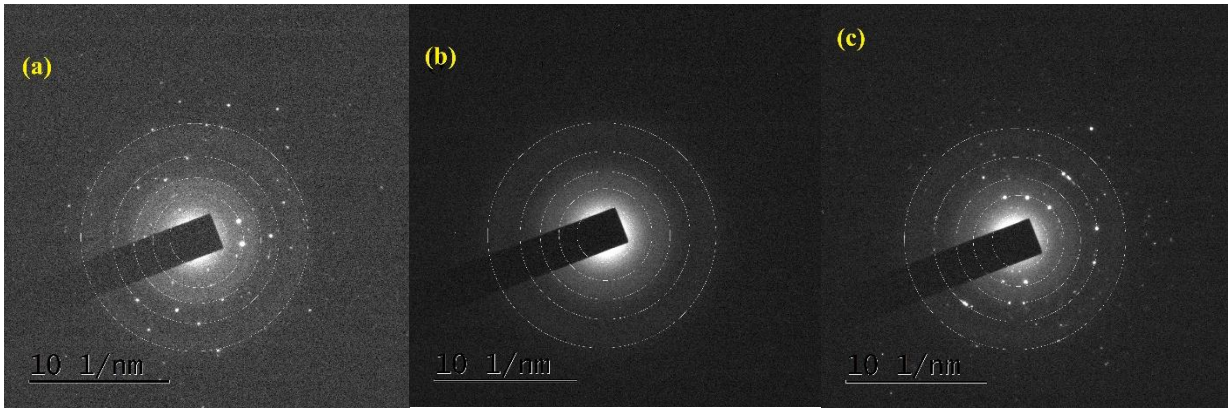



**Figure 16.** SAED patterns of (a) MF, (b) MF/PANI, (c) MF/CS nanocomposites

**Energy Dispersive X-ray Analysis (EDAX)**

The chemical composition of the composites including $MnFe_2O_4$, $MnFe_2O_4$/PANI, $MnFe_2O_4$/CS was investigated through EDAX analysis which generally provides with the qualitative and

quantitative information of the elements (Hema and Revathi 2024). As shown in the Fig.17 EDS measurement of the pure MF confirmed the presence of Mn, Fe, O where the atomic ratio of Mn:Fe is 1:2 stoichiometry which confirms the formation spinel metal ferrite. And for MF/PANI composite (Fig.18), additionally C, N was observed along with the basic Mn, Fe, O peaks indicating the successful incorporation of the polyaniline onto the metal ferrite nanoparticles. Similarly, MF/CS composite (Fig.19), the peaks for chitosan, biopolymer matrix which includes C, N along with the Mn, Fe, O peaks confirmed the encapsulation of the biopolymer onto the metal ferrite network. The relative decrease in the atomic weight percentage of Mn and Fe in the polymer-based composites indicates the successful incorporation of polymers into the $MnFe_2O_4$ (Banaei et al. 2024).

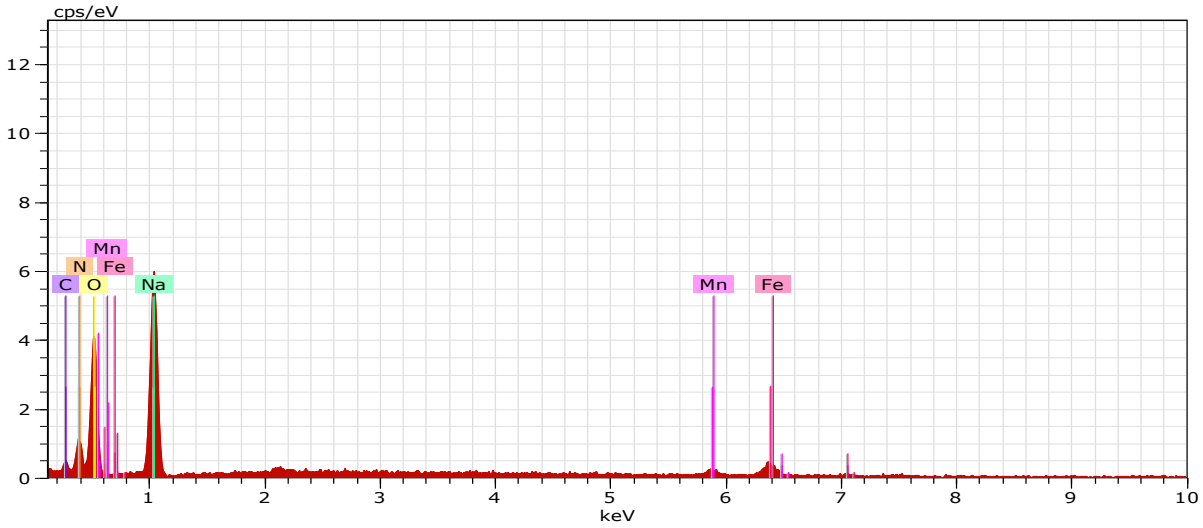



**Figure 17.** EDAX analysis of $MnFe_2O_4$

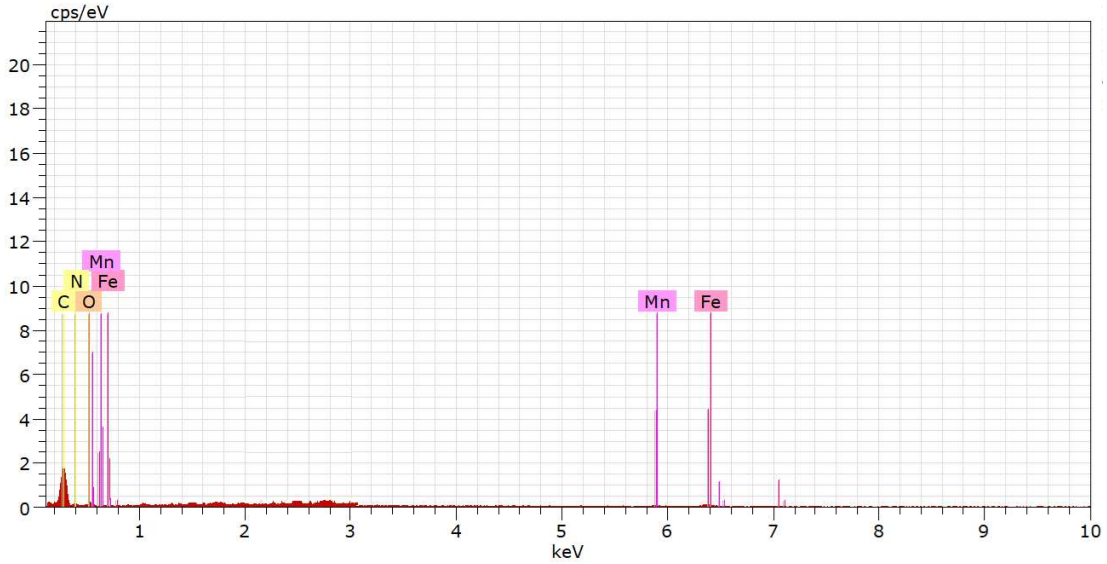



**Figure 18.** EDAX analysis of $MnFe_2O_4$/PANI composite

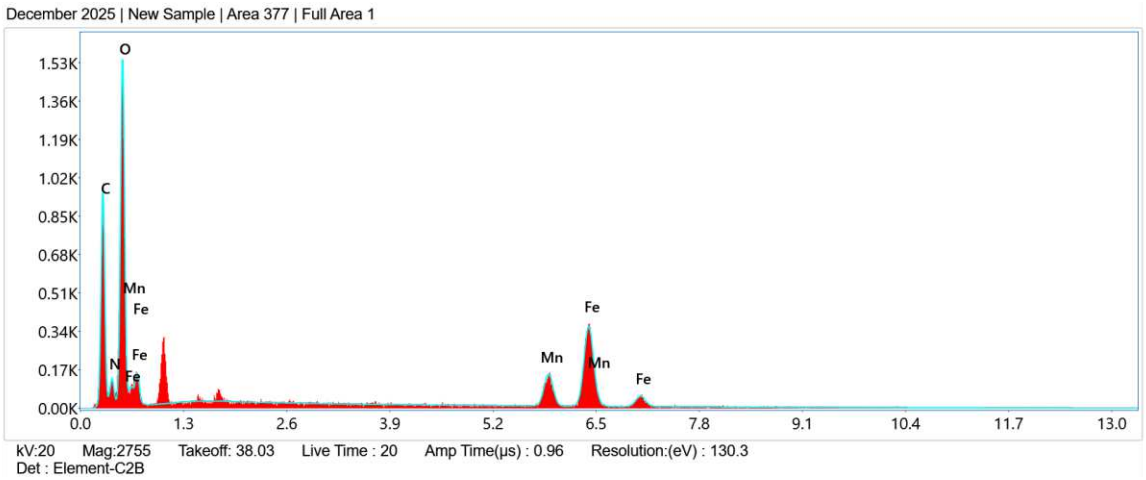



**Figure 19.** EDAX analysis of $MnFe_2O_4$/CS composite

## 2.5.UV-DRS Spectroscopy

The UV-Visible Reflectance Spectroscopy was carried out to obtain the bandgap energy values for MF, MF/PANI, MF/CS (Fig.20 a, b, c) which shows the catalytic activity of the compounds. the Kubelka-Munk approach were employed to find out the bandgap energy values from the recorded UV-DRS data, the Kubelka-Munk function F(R)=k/S, where k is the absorption coefficient and S is the scattering coefficient, were used for the bandgap estimation. The optical bandgap energy values are found out using Tauc plots with indirect allowed transition. And the calculated bandgap energy values were found to be $E_g$= 3.36eV for MF, $E_g$= for 3.08eV MF/PANI, $E_g$= 5.15eV for MF/CS. The indirect transition fit was selected because of the good linearity and the typical nature of the spinel ferrites exhibiting indirect transition to be prominent.

UV-DRS analysis reveals that upon polymer incorporation with $MnFe_2O_4$, it shows electronic oscillation. Where MF/PANI exhibited reduced bandgap energy (Chen et al. 2015) than pure MF, which is due to the strong interfacial interaction and the π-conjugation of the conducting polyaniline backbone that results in the formation of intermediate energy states that narrow the optical bandgap (Saoudi et al. 2021). On the other hand, chitosan is insulating and non-conjugated and suppresses electronic interaction with the ferrite lattice and creates a di-electric coating effect which results with the considerable increase in the bandgap energy value in the MF/CS composite (Varghese et al. 2022) (Morgado et al. 2013).

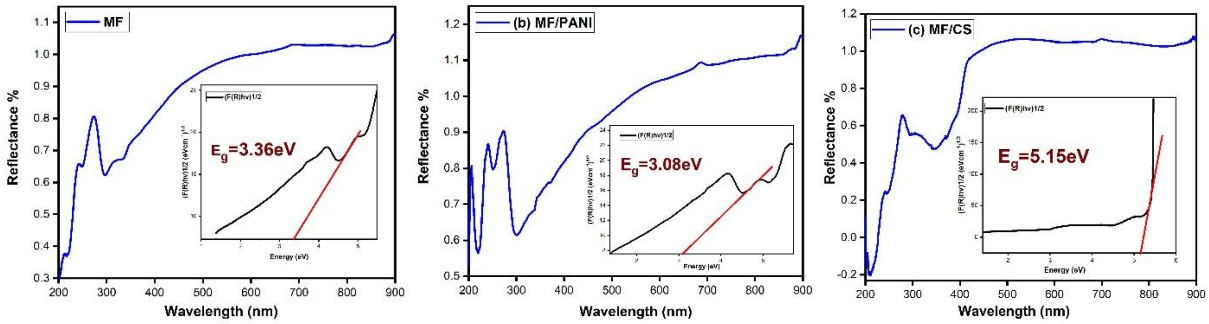



**Figure 20.** UV-DRS spectrum and energy bandgap of as-synthesized (a) MF, (b) MF/PANI, (c) MF/CS nanocomposites using Tauc plot method

## 2.6.Photonic and non-photonic UV Analysis in degradation Acid Orange 10 dye

The catalytic dye degradation of acid orange 10 dye (AO10), using MF, MF/PANI, MF/CS catalysts was recorded using UV-Visible spectroscopy. AO10 dye exhibits the maximum absorbance value of 475 nm, which corresponds to the (-N=N-) azo bonds in the dye. Fig. 21 Represents the time dependent UV-Visible absorbance spectra, recorded in the presence of both photonic and non-photonic catalysts. For MF (photonic catalyst), UV-photo reactor is utilized throughout their degradation process, in contrast for MF/PANI, MF/CS (non-photonic catalysts) magnetic stirrer is used under dark condition, where the data is recorded with the respective time interval using UV-Visible spectroscopy. A progressive decrease in the absorbance with respect to the λ (nm) shows the effective degradation of the azo dye, acid orange 10. In this study we prepared the stock solution of 20mg/L Acid orange 10 dye in a litre of double distilled water and stored them in the dark and kept this concentration constant throughout the experiment. The photonic and non-photonic degradation efficiency % is calculated using the equation(Wagh et al. 2024).

$$\text{Degradation efficiency \%} = ((C_O - C_t)/C_O) \times 100 \qquad \textbf{(Eqn. 2)}$$

$$\text{Degradation efficiency \%} = \frac{C_o - C_t}{C_o} \times 100$$

Where $C_o$ is the absorbance at time t= 0 min and $C_t$ is the absorbance at time 't' min.

The photonic catalyst MF showed the degradation efficiency of 65.16% in 20 min and the non-photonic atalyst MF/PANI and MF/CS degraded the dye with 98% and 94% under dark stirring conditions in 6 mins and 14 mins effectively.

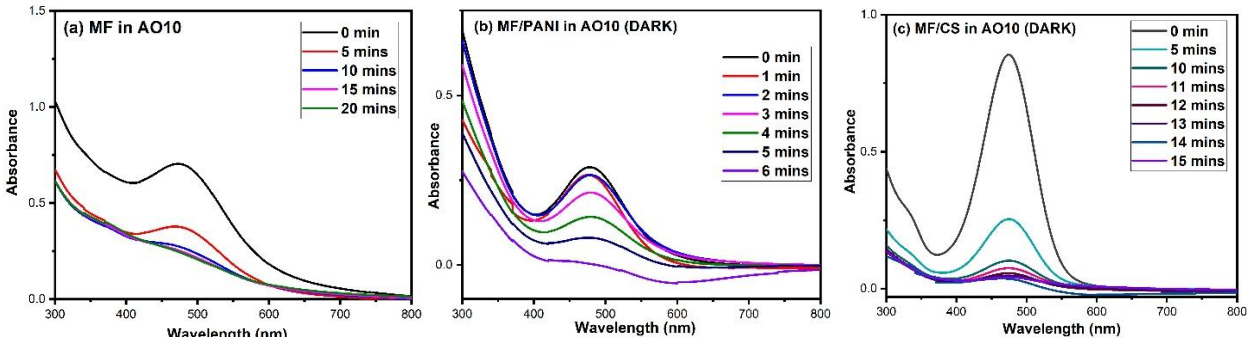



**Figure 21.** UV-Vis spectra showing Photonic and non-photonic degradation of AO10 DYE at 20mg/L (a) MF, (b) MF/PANI, (c) MF/CS nanocomposites

**Effect of catalyst dosage**

The effect of catalyst dosage on AO10 degaradtion efficiency was calculated by varyin with 0.01g, 0.02g, 0.03g to 20mg$L^{-1}$ as the constant dye concentration. The Fig.22a represents the catalyst dosage variation of the catalysts against degradation efficiency. An increase in the degaradtion efficiency with decreasing catalyst dosage was observed, and with higher dosages no significant improvement in degradation % was noted. Based on the results, 0.01g for MF and MF/PANI and 0.02g for MF/CS was chosen as the optimum dosage for the further experiments. The Table 1. represents the catalyst dosages and the degradation efficiency % for MF, MF/PANI, MF/CS. And the Fig.22a depicts the plot to determine the degradation efficiency % at the selected catalyst dosages. And the Table 1. Shows the effective degradation efficiency of the catalysts at the varied dosages.

**Table 1.** Table of degradation efficiency for the varied catalyst dosages of MF, MF/PANI, MF/CS

| **Sample / Dosage** | **Degaradation efficiency %** | | |
|---|---|---|---|
| | 0.01g | 0.02g | 0.03g |
| **MF** | 64.97 | 47.55 | 40.93 |
| **MF/PANI** | 98.59 | 89.64 | 70.5 |
| **MF/CS** | 62.92 | 95.78 | 87.65 |

**Effect of pH on degradation efficiency**

Effect of pH on dye degradation plays an important role by influencing the efficieny of the degradation processess. It affects the reactive species generation, stability of intermediates and also the degradation rates of the dyes. Generally, acidic conditions favor the degardation of dyes (Che Zulzikrami et al. 2014), but the optimal pH may vary depending on the dye and the synthesis method used (Tum 2022). As shown in the Fig.22b the maximum degradation efficieny was achieved at pH 5 for MF and pH 3 for MF/PANI and MF/CS. The electrostatic attraction to the catalyst surface is enhanced by the dye molecules under acidic conditions which facilitates the faster degradation of the dye. Fig.22b Illustrates the degaradation efficiency % with respect to pH

at the selected catalyst dosages. And Fig.22c represents the maximum removal of the azo dye at the selected catalyst dosages and the pH.

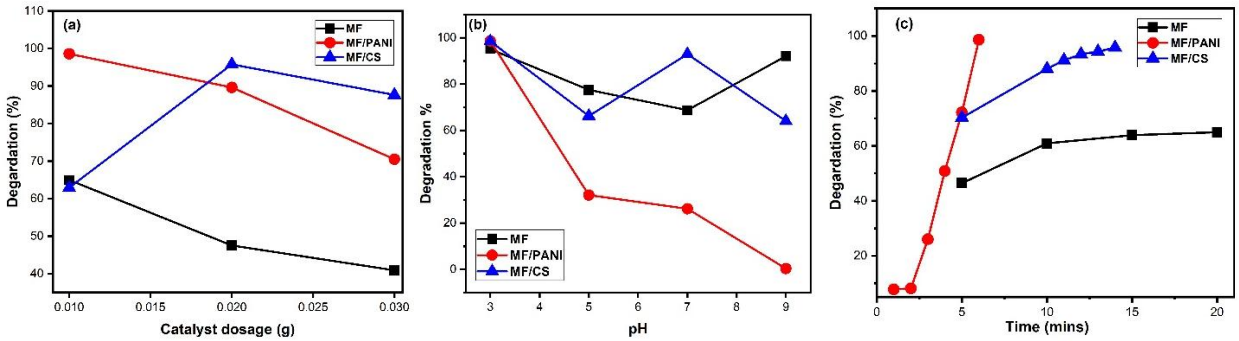



**Figure 22.** (a) Effect of catalyst dosage, (b) Effect of pH and (c) degradation efficiency plots of MF, MF/PANI, MF/CS nanocomposites against acid orange 10 azo dye

**Kinetic analysis**

Fig.23 represents the graph plotted for $C_o/C_t$ vs time 't'. The kinetic behaviour was evaluated by plotting $\ln(C_o/C_t)$ vs time 't' (Fig. 24) Where $C_o$ and C represents the initial and time-dependent dye concentrations respectively. All the catalyst exhibited the very well linearity which confirms the suitability of the pseudo first order kinetic model. The rate constants (k) and the coefficient of determination ($R^2$) obtained from the fitted slopes are listed in Table 2. which indicates the fitting accuracy towards the pseudo first order kinetic model.

Among all the three catalysts MF/PANI non-photonic catalyst exhibited the highest degradation rate constant due to the presence of conducting polyaniline network which promotes the rapid electron transfer and acceleration of the redox cycling between $Mn^{3+}/Mn^{2+}$ and $Fe^{3+}/Fe^{2+}$. The MF/CS composite also showed high rate constant with $R^2$ value of 0.99087, which suggests that strong dye adsorption and surface mediated redox reactions control the degaradation process under acidic condition. In contrast, the $MnFe_2O_4$ showed slower kinetics when compared to polymer modified composites which shows its limited adsorption capacity and less electron-charge transfer pathways. Collectively, the kinetic results reveals that the polymer modified composites shows the enhanced degradation effieciency % in the following order:

**MF/PANI > MF/CS >> MF**

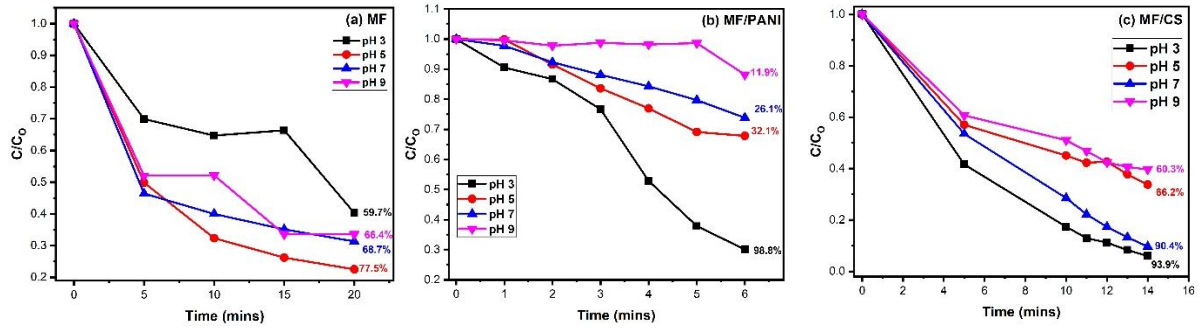



**Figure 23.** Graph of $C_o/C_t$ vs time for (a) MF, (b) MF/PANI, (c) MF/CS nanocomposites

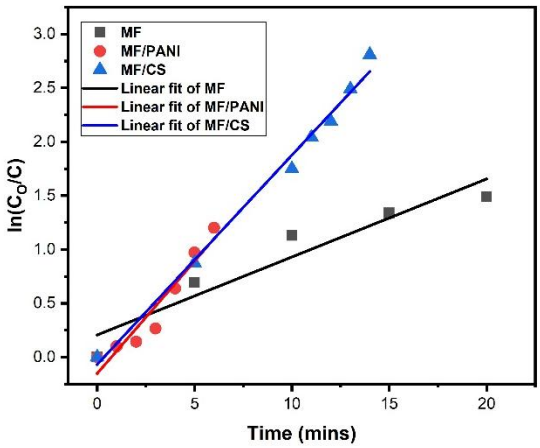



**Figure 24.** Graph of $\ln(C_o/C_t)$ vs time for (a) MF, (b) MF/PANI, (c) MF/CS nanocomposites

**Table 2.** Observed first order rate constant of the photonic and non-photonic reaction, k_obs

| **Sample** | **MF** | **MF/PANI** | **MF/CS** |
|---|---|---|---|
| **pH** | 5 | 3 | 3 |
| **Intercept** | 0.20575 ± 0.15936 | -0.15165 ± 0.09717 | -0.06822 ± 0.08668 |
| **Slope** | 0.07248 ± 0.01301 | 0.20852 ± 0.02695 | 0.19441 ± 0.00835 |
| **R-Square** | 0.91183 | 0.92292 | 0.99087 |

## Mechanism

In case of pristine $MnFe_2O_4$, they posses a mixed valence metal ions $Mn^{3+}/Mn^{2+}$ and $Fe^{3+}/Fe^{2+}$ which participates in the redox reactions (Eqn.3). The electrons from the dye molecules are trasnferred to these metal ions after adsorption which results in the partial reduction of $Mn^{3+}$ and $Fe^{3+}$ ions.

$$Mn^{3+}/Fe^{3+} + e^- \text{ ---> } Mn^{2+}/Fe^{2+} \qquad \textbf{(Eqn.3 )}$$

These reduced metal ions react with the dissolved oxygen and generate reactive oxygen species scuh as superoxide radical ($\bullet O_2^-$) and hydroxyl radicals (•OH) which cleaves the azo bond in the acid orange 10 dye resulting with the dye adsorption from aqueous solution.

For MF/PANI composite, the degardation mechanism is enhanced due to the presence of conducting polyaniline matrix, which gets protonated under acidic conditions providing with the positively charged sites that strongly attracts the anionic dye molecules. Polyaniline being an effective electron-transfer intermediate facilitates the rapid movement of electrons from the dye molecules to the Mn and Fe redox sites. Even in the absence of light, this speeds up the redox cycles of $Mn^{3+}/Mn^{2+}$ and $Fe^{3+}/Fe^{2+}$.

In MF/CS composite, the strong adsorption capacity of chitosan prominently increases the degradation process. Under acidic conditions the amine groups of the chitosan are protonated, which creates the positively charged sites that binds with the negatively charged sites of the dye molecules. In both polymer modified composites, even in the absence of light the dissolved oxygen react with the metal ions and the reactive oxygen species formed in dark attacks the azo bond in the dye, leading to the breakage of chromophore and formation of the smaller aromatic fragments and further oxidized to $CO_2$, $H_2O$ and other inorganic ions as the final degraded products. Both conducting and bio-polymer-modified ferrite composites can be further utilized for efficent dye degradation of various dyes. While the MF/PANI composite exhibited high catalytic activity at the lower dosage due to its enhanced charge transport, the MF/CS composite required a higher catalyst dosage that is twice the amount of MF/PANI to result with equivalent degradation efficiency which are due to the eco-friendly nature and the biopolymer backbone.

The rapid breakdown of AO10 under both photonic and non-photonic conditions is made possible by the synergitic connection between $MnFe_2O_4$ and the polymers, which truly demonstrates the future potential of these composites for advanced waste water treatment applications.

**2.7.Brunauer-Emmett-Teller Analysis (BET)**

Fig. 25 Shows the $N_2$ adsorption-desorption isotherms of $MnFe_2O_4$, MF/PANI, MF/CS nanocomposites which confirms the mesoporous nature of the nanocomposites. All the catalysts exhibited Type IV isotherm with H3 hysteresis loop in the $P/P_O$ range of 0.4-1 which are finalized based on the International Union of Pure and Applied Chemistry classification that shows the nature of mesoporous structures (Jiang et al. 2024; Shih and Tseng 2025). The Barrett-Joyner-Halenda (BJH) pore size analysis (insets in Fig.25 shows the pore size of 8.88, 9.21, 3.15 nm and a pore volume of 0.2136, 0.0431, 0.0113 $cm^3/g$ respectively. And the BET surface area for MF, MF/PANI, MF/CS is measured as 96.21, 18.72, 14.29 $m^2/g$.

The surface area measurements are reported in the Table 3. The BET surface area is the highest for $MnFe_2O_4$. While the polymer incorporated $MnFe_2O_4$ exhibited the lower surface area values but retained the mesoporous structure which rules the dye removal performance. Thus, BET analysis revealed a significant decrease in the surface area and pore volume upon polymer loading, which is related to incorporation and partial pore blocking of $MnFe_2O_4$ by polyaniline and chitosan. Still, even with the lower BET surface area, the polymer-modified composites exhibited drastic enhancement in the dye adsorption under dark conditions. This behavior emerges from the presence of protonated amines and the hydroxyl functional groups which enables strong

electrostatic interactions, hydrogen bonding and π-π interactions with the anionic dye molecules (Rout and Jena 2024). As a result, dye removal in polymer-modified systems is governed mainly by chemical affinity rather than the physical surface area.

**Table 3.** Physical parameters of MF, MF/PANI, MF/CS

| Catalyst | BET surface area ($m^2/g$) | Average pore diameter (nm) | Total pore volume ($cm^3/g$) |
|---|---|---|---|
| MF | 96.21 | 8.88 | 0.2136 |
| MF/PANI | 18.72 | 9.21 | 0.0431 |
| MF/CS | 14.29 | 3.15 | 0.0113 |

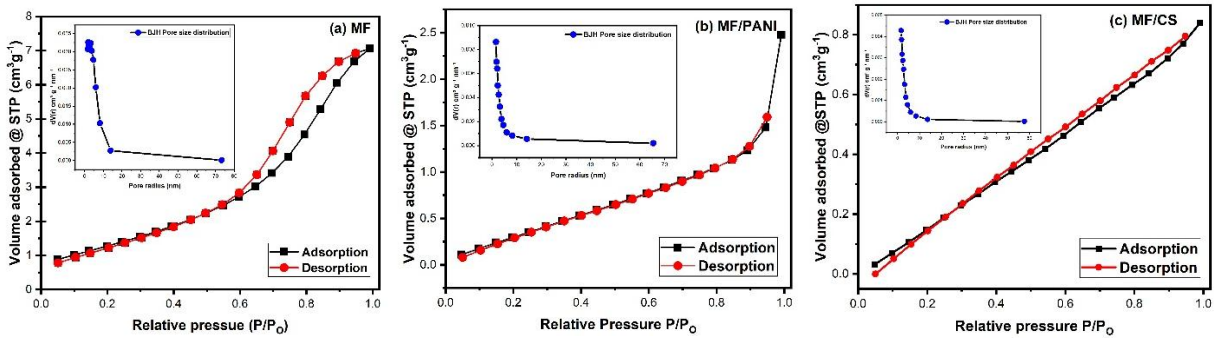



**Figure 25.** $N_2$ adsorption-desorption isotherms and BJH pore size analyses for (a) MF, (b) MF/PANI, (c) MF/CS nanocomposites

**Comparative evaluation with reported studies**

To highlight the efficiency of the present polymer-modified Manganese ferrite systems, a comparative evaluation with previously reported dye degradation studies is presented in the Table 4 below. The parameters such as catalyst dosage, light condition, degradation efficiency and the time required to degrade are compared to show the performance of the present work.

**Table 4.** Comparative Evaluation of acid orange dye degradation performance with previously reported studies

| Catalyst | Dye | Light condition | Dosage | Degradation % | Time (mins) | Ref |
|---|---|---|---|---|---|---|
| $TiO_2$ | Acid Orange II (AO7) | UV-Photoreactor | 0.1 g/L | 97% | 120 min | (Salima BENDE BANE 2026) |
| $TiO_2$ | Acid Orange 10 | UV-Photoreactor | 0.1–1 g/L | 95% | 300 mins | (Abbas and Trari 2022) |
| Sn(IV)-porphyrin-based catalysts | Acid Orange 07 | UV-Photoreactor | 10mg | 86% to 91% | 90 min | (Shee and Kim 2022) |

| | | | | | | |
|---|---|---|---|---|---|---|
| $CaO\text{-}MnFe_2O_4$ | methylene blue | UV-Photoreactor | 0.03 g | 86 % | 240 min | (Rodiah and Ramadhani 2022) |
| $MnFe_2O_4$ | Acid Orange 10 | UV-Photoreactor | 0.01g | 65% | 20 min | This work |
| $MnFe_2O_4$/ polyaniline | Acid Orange 10 | Dark, Room temperature | 0.01g | 98.5% | 6 mins | This work |
| $MnFe_2O_4$/ Chitosan | Acid Orange 10 | Dark, Room temperature | 0.02g | 95.8% | 14 mins | This work |

## Conclusion

In this study, $MnFe_2O_4$ (MF), $MnFe_2O_4$/Polyaniline (MF/PANI), $MnFe_2O_4$/Chitosan (MF/CS) composites were successfully utilised for the degradation of the azo dye acid oragne 10 under both photonic and non-photonic conditions. X-ray diffraction revealed the formation of well defined spinel ferrite phase and also the confirmation of successful polymer incoporation without and phase distortion. FTIR analysis represented the metal-oxygen vibrations along with the polymer functional groups which indicate the strong interfacial interactions between pure $MnFe_2O_4$ and the polymers. XPS analysis confirms the presence of $Mn^{3+}/Mn^{2+}$ and $Fe^{3+}/Fe^{2+}$ species in the spinel ferrite lattice and the C, N, O signals validates the successful incorporation of polyaniline and chitosan. HRTEM images revealed the formation of well defined $MnFe_2O_4$ nanrods and also the uniformly incorporated polymers into the nanrods in the composites. And the SAED patterns of all the composites shows the concentric diffraction rings indexed to the cubic spinel ferrite which confirms the phase purity and poly-crystallinity. The $N_2$ adsorption-desorption studies revealed the Type-IV isotherms with hysteresis loops for all the samples which confirms its mesoporous structure. And also a comparative evaluation with previously reported studies highlights the efficiency of the polymer-modified composites under dark conditions. In summary, this study demonstrates how the polymer modified $MnFe_2O_4$ composites work as efficient non-photonic catalysts to breakdown hazardous azo dye from aqueous solution. This excellent catalytic performance makes them the promising candidates for real and sustainable waste water treatment applications.

**References**


Abbas M, Trari M (2022) Application of photocatalysis for the decontamination of water contaminated with the Acid Orange 10 dye in the presence of TiO2 under irradiation. Desalination and Water Treatment 250:288–297

Abdollahi F, Yousefi M, Hekmati M, Khajehnezhad A, Afghahi S S S, (2020) Adsorption and photodegrading of Methylene Blue by using of BaLaxGdxFe12-2xO19 (x= 0.2, 0.4, 0.6 and 0.8)/PANI nanocomposites. International Journal of Nano Dimension 11:

Akter F, Dong Y (2024) Investigation of removing orange II azo dye from wastewater through an oxidation process. Applied Water Science 14:243

Banaei A, Saadat A, Gharibzadeh N, Ghasemi PP (2024) Synthesis and characterization of new composite from modified silica-coated $MnFe_2O_4$ nanoparticles for removal of tetracycline from aqueous solution. RSC Adv 14:14170–14184. https://doi.org/10.1039/D4RA01007H

Biesinger MC, Payne BP, Grosvenor AP, Lau L.W, Gerson A R, Smart R S C, (2011) Resolving surface chemical states in XPS analysis of first row transition metals, oxides and hydroxides: Cr, Mn, Fe, Co and Ni. Applied Surface Science 257:2717–2730

Che Zulzikrami A, Muhammad Ridwan Fahmi MRF, Ong SoonAn OS, Nazerry Rosmady Rahmat N.R.R., Siti Nurfatin N M M and Razi Ahmad R A, (2014) Effect of pH and H2O2 dosage on the photooxidative degradation of Reactive Red 120 (RR120) by UV-H2O2.

Chen B, Long F, Chen S, Cao Y, Pan X, (2020) Magnetic chitosan biopolymer as a versatile adsorbent for simultaneous and synergistic removal of different sorts of dyestuffs from simulated wastewater. Chemical Engineering Journal 385:123926

Chen X, Jiang J, Liang Q, Yang N, Ye H Y, Cai M, Shen L, Yang D G and Ren T L, (2015) First-principles study of the effect of functional groups on polyaniline backbone. Scientific reports 5:16907

Das P, Debnath A, Saha B (2020) Ultrasound-assisted enhanced and rapid uptake of anionic dyes from the binary system onto MnFe2O4/polyaniline nanocomposite at neutral pH. Applied Organometallic Chemistry 34:e5711

Devi E, Soibam I (2017) Structural and optical characterization of MnFe2O4 nanoparticles. pp 93–96

Doğan M (2020) Preparation of chitosan nanoparticles and characterization studies. Cumhuriyet Medical Journal 42:

Duarte F da S, Melo ALM dos S, Ferro A de B, Zanta C L D P E S, Duarte J L D S and Oliveira R M P B, (2022) Magnetic zinc oxide/manganese ferrite composite for photodegradation of the antibiotic rifampicin. Materials 15:8185

Giannousi K, Toursidis PD, Chatzatoglou E, Dendrinou-Samara C (2025) Manganese Ferrite Nanoparticles functionalized with gallic acid for inhibition of insulin amyloids formation and mitigation of oxidative stress. Colloids and Surfaces A: Physicochemical and Engineering Aspects 138114

Grosvenor A, Kobe B, Biesinger MC, McIntyre N (2004) Investigation of multiplet splitting of Fe 2p XPS spectra and bonding in iron compounds. Surface and Interface Analysis: An International Journal devoted to the development and application of techniques for the analysis of surfaces, interfaces and thin films 36:1564–1574

Hema P, Revathi V (2024) Durability Evaluation of GGBS-RHA-Based Geopolymer Concrete Along with Lightweight Expanded Clay Aggregate Using SEM Images and EDAX Analysis. Buildings 14:3355. https://doi.org/10.3390/buildings14113355

Ilosvai ÁM, Heydari F, Forgách L, Kovács N, Szigeti K, Máthé D, Kristály F, Daróczi L, Viskolcz B, Nagy M and Németh M, (2025) Development of manganese ferrite coated with Prussian blue as an efficient contrast agent for applications in magnetic resonance imaging. Scientific Reports 15:14150

Itodo H, Nnamonu L, Wuana R (2017) Green synthesis of copper chitosan nanoparticles for controlled release of pendimethalin. Asian Journal of Chemical Sciences 2:1–10

Jiang X, Tan Z, Jiang G, Liu C, Gao G and Liu Z, (2024) Novel Magnetic MnFe2O4-decorated graphite-like porous biochar as a heterogeneous catalyst for activation of peroxydisulfate toward degradation of rhodamine B. ACS omega 9:6455–6465

Khilari S, Pandit S, Varanasi JL, Das D and Pradhan D, (2015) Bifunctional manganese ferrite/polyaniline hybrid as electrode material for enhanced energy recovery in microbial fuel cell. ACS Applied Materials & Interfaces 7:20657–20666

Kolhar P, Sannakki B, Verma M, SV P, Alshehri M Shah, NA, (2023) Synthesis, characterization and investigation of optical and electrical properties of polyaniline/nickel ferrite composites. Nanomaterials 13:2223

Lahouti S, Naeimi H (2020) Chitosan-encapsulated manganese ferrite particles bearing sulfonic acid group catalyzed efficient synthesis of spiro indenoquinoxalines. RSC advances 10:33334–33343

Manohar A, Suvarna T, Vattikuti SP, Almunyif A A, Sangaraju S, Kim K H, (2025) Comprehensive study on the physical and electrochemical behavior of $Mn_{0.4}Mg_{0.6}Fe_2O_4/CeO_2/MnFe_2O_4$ nanocomposite for energy storage applications. Colloids and Surfaces A: Physicochemical and Engineering Aspects 137748

Meng F, Wang X, Jiang D, Ma R (2016) Microwave Absorbing and Magnetic Properties of the Polyaniline. Materials Science 22:

Mohammad Hosseini N, Sheshmani S, Shahvelayati AS (2025) Manganese ferrite-graphite oxide-chitosan nanocomposite for efficient dye removal from aqueous and textile wastewater under UV and sunlight irradiation. Scientific Reports 15:866

Molapo KM, Ndangili PM, Ajayi RF, Mbambisa G, Mailu S M, Njomo N, Masikini M and Iwuoha P B I, (2012) Electronics of conjugated polymers (I): polyaniline. International Journal of Electrochemical Science 7:11859–11875

Morgado J, Pereira A, Bragança A, Ferreira Q, Fernandes S C, Freire C S R, Silvestre A J D, Neto C P and Alcácer L, (2013) Self-standing chitosan films as dielectrics in organic thin-film transistors. Express Polym Lett 7:960–965

Murugesan C, Ugendar K, Okrasa L, Shen J and Chandrasekaran G, (2021) Zinc substitution effect on the structural, spectroscopic and electrical properties of nanocrystalline MnFe2O4 spinel ferrite. Ceramics International 47:1672–1685

Nessaibia M, Ghodbane H, Ferkous H, Merouani S, Alam M, Balsamo M, Benguerba Y and Erto A, (2023) Homogenous UV/periodate process for the treatment of acid orange 10 polluted water. Water 15:758

Patil PH, Kulkarni VV, Dongale TD, Jadhav SA (2023) α-Manganese dioxide (α-MnO2) coated with polyaniline (PANI) and reduced graphene oxide (rGO)-based nanocomposite for supercapacitor application. Journal of Composites Science 7:167

Peleyeju MG, Arotiba OA (2018) Recent trend in visible-light photoelectrocatalytic systems for degradation of organic contaminants in water/wastewater. Environmental Science: Water Research & Technology 4:1389–1411

Rodiah S, Ramadhani E (2022) Highly efficient removal of methylene blue dye from wastewater using CaO-MnFe2O4 nanoparticles prepared with teak leaf extract. al Kimiya: Jurnal Ilmu Kimia dan Terapan 9:62–67

Rout DR, Jena HM (2024) Chitosan cross-linked polyaniline grafted graphene oxide composite: a new adsorbent to remove phenol and cationic dye from aqueous solutions. International Journal of Environmental Analytical Chemistry 104:3800–3820

Salima BENDEBANE CS (2026) Intensified UV/TiO2 Photocatalytic Treatment of Colored Wastewater: Acid Orange 10 Removal in Closed and Semi-Closed Reactors. Global NEST Journal. https://doi.org/10.30955/gnj.08233

Sambhudevan S (2021) Ferrite-based polymer nanocomposites as shielding materials: A review. Chemical Papers 75:3697–3710

Saoudi M, Zaidi B, Alotaibi AA, Althobaiti M G, Alosime E M and Ajjel R, (2021) Polyaniline: doping and functionalization with single walled carbon nanotubes for photovoltaic and photocatalytic application. Polymers 13:2595

Shee NK, Kim H-J (2022) Sn (IV)-Porphyrin-Based Nanostructures Featuring Pd (II)-Mediated Supramolecular Arrays and Their Photocatalytic Degradation of Acid Orange 7 Dye. International Journal of Molecular Sciences 23:13702

Shih K-Y, Tseng H-Y (2025) One-Step Microwave-Assisted Synthesis of MnFe2O4/rGO Nanocomposites and Their Electrochemical Properties in Supercapacitors. ACS omega 10:4473–4485

Skliri E, Vamvasakis I, Papadas IT, Choulis S A and Armatas G S, (2021) Mesoporous composite networks of linked MnFe2O4 and ZnFe2O4 nanoparticles as efficient photocatalysts for the reduction of Cr (VI). Catalysts 11:199

Suresh S, Deshmukh SA, Bhuse DV, Mallesham B and Nagapillai P, (2025) Review on magnetically retrievable spinel ferrites MFe2O4/TiO2 (M= Co, Zn) composites and its application for photocatalytic removal of pollutants. Applied Water Science 15:284

Tum PK (2022) Rate of Photocatalytic Degradation of Acid Orange 7 Azo Dye on TiO2 Coated Layers: Role of pH and Initial Dye Concentration. International Journal of Innovative Research and Development 11:

Varghese AA, Kuriakose E, Jose J, Aryal S, Khanal R and Anila E I, (2022) Investigations on the electronic properties and effect of chitosan capping on the structural and optical properties of zinc aluminate quantum dots. Applied Surface Science 579:152162

Vieira RS, Oliveira MLM, Guibal E, Rodríguez-Castellón E and Beppu M M, (2011) Copper, mercury and chromium adsorption on natural and crosslinked chitosan films: An XPS investigation of mechanism. Colloids and Surfaces A: Physicochemical and Engineering Aspects 374:108–114

Vigneshwari S, Gokula V Extraction and FTIR characterization of chitosan from Portunus pelagicus (Linnaeus, 1758) shell wastes

Wagh SS, Chougale AS, Survase AA, Patil R S, Naik N, Naushad M and Pathan H M, (2024) Rapid photocatalytic dye degradation, enhanced antibacterial and antifungal activities of silver stacked zinc oxide garnished on carbon nanotubes. Scientific Reports 14:14045

Xiao Y, Liang H, Wang Z (2013) MnFe2O4/chitosan nanocomposites as a recyclable adsorbent for the removal of hexavalent chromium. Materials Research Bulletin 48:3910–3915

Zeng S, Yang J, Qiu X, Liang Z and Zhang Y, (2016) Magnetically recyclable MnFe2O4/polyaniline composite with enhanced visible light photocatalytic activity for rhodamine B degradation. Journal of the Ceramic Society of Japan 124:1152–1156

Zolfaghari Y, Ghorbani M, Lashkenari MS (2021) Electrochemical study on zeolitic imidazolate framework-67 modified MnFe2O4/CNT nanocomposite for supercapacitor electrode. Electrochimica Acta 380:138234

**Acknowledgment**

The authors gratefully acknowledge the DST-FIST fund for providing the UV-Visible spectrophotometer facility utilized in this study.

**Funding**

The authors declare that no funding was received for this work.

**Authors' contributions**

Hepzibah Anto performed the experiments, analyzed the data and wrote the manuscript. Dr. Rajakani Paramasivam supervised the research work and reviewed the manuscript and Dr. Chinnapiyan Vedhi assisted in manuscript editing and guided during experiments. All authors approved the final manuscript.

**Ethical approval**

Not applicable.

**Consent to participate**

Not applicable.

**Consent to Publish**

All authors agree to publish this manuscript.

**Competing interests**

The authors declare no competing interests.

**Data Availability**

The data that support the findings of this study are available on request from the corresponding author.